Nanoscale

PAPER

View Article Online
View Journal | View Issue

Cite this: *Nanoscale*, 2023, **15**, 18291

The central core size effect in quinoxaline-based non-fullerene acceptors for high V_{OC} organic solar cells†

Xinya Ran,‡[a,b] Yanan Shi,‡[a] Dingding Qiu,[a,b] Jianqi Zhang,[a] Kun Lu *[a,b] and Zhixiang Wei[a,b]

For organic solar cells (OSCs), obtaining a high open circuit voltage (V_{OC}) is often accompanied by the sacrifice of the circuit current density (J_{SC}) and filling factor (FF), and it is difficult to strike a balance between V_{OC} and J_{SC} × FF. The trade-off of these parameters is often the critical factor limiting the improvement of the power conversion efficiency (PCE). Extended backbone conjugation and side chain engineering of non-fullerene acceptors (NFAs) are effective strategies to optimize the performance of OSCs. Herein, based on the quinoxaline central core and branched alkyl chains at the β position of the thiophene unit, we designed and synthesized three NFAs with different sized cores. Interestingly, **Qx-BO-3** with a smaller central core showed better planarity and more appropriate crystallinity. As a result, PM6:**Qx-BO-3**-based devices obtained more suitable phase separation, more efficient exciton dissociation, and charge transport properties. Therefore, the OSCs based on PM6:**Qx-BO-3** yielded an outstanding PCE of 17.03%, significantly higher than the devices based on PM6:**Qx-BO-1** (10.57%) and PM6:**Qx-BO-2** (11.34%) although the latter two devices have lower V_{OC} losses. These results indicated that fine-tuning the central core size can effectively optimize the molecular geometry of NFAs and the film morphology of OSCs. This work provides an effective method for designing high-performance NFA-OSCs with high V_{OC}s.

Received 9th October 2023,
Accepted 25th October 2023

DOI: 10.1039/d3nr05077g

rsc.li/nanoscale

1. Introduction

Organic solar cells (OSCs) are considered to be one of the most promising emerging photovoltaic technologies due to their advantages of low cost, flexibility, transparency, and solution processing.[1–6] With material innovation, device optimization, and mechanism studies, OSCs have witnessed significant progress in the past decade and achieved power conversion efficiencies (PCEs) of over 19% and 20% for single junction and tandem devices, respectively.[7–16] However, it is still a challenge to comprehend the relationship between the molecular structure of NFAs and their photovoltaic performance and to achieve a balance among the various parameters influencing the PCE of OSCs.[17–19]

As one of the most successful NFAs, Y6 possesses a unique banana-like configuration with an A–DA′D–A architecture and achieved a PCE breakthrough of 15.7%.[20] Numerous innovative studies have been conducted to enhance the device performance through structural modifications of Y-series acceptors.[21–27] In OSCs, a high energy loss (E_{loss}) often leads to limited V_{OC}, consequently, and extending the conjugated backbone is widely recognized as an effective approach to achieve a superior V_{OC}.[28–30] A series of studies have introduced quinoxaline-fused cores instead of the traditional benzothiadiazole (BTZ)-fused cores in Y-series acceptors, resulting in the creation of quinoxaline (Qx)-series acceptors.[31–33] The Qx-series NFAs possess various advantages, such as enhanced molecular rigidity, additional chemical modification sites, and reduced non-radiation energy loss.[34,35] For instance, Zhu *et al.* reported AQx-series NFAs that incorporate quinoxaline-fused cores. They found that the reductive phase-separated morphology enhances hole transfer and suppresses geminate recombination. Therefore, a high PCE of 16.64% was achieved in binary OSCs.[36] Wei *et al.* reported that by suppressing the molecular vibration of the C–C bond stretching of Qx-series molecules, the E_{loss} caused by exciton dissociation and nonradiative recombination was significantly reduced.[37] These efforts

[a]*CAS Key Laboratory of Nanosystem and Hierarchical Fabrication, CAS Center for Excellence in Nanoscience, National Center for Nanoscience and Technology, Beijing 100190, China. E-mail: lvk@nanoctr.cn*
[b]*Sino-Danish Center for Education and Research, Sino-Danish College University of Chinese Academy of Sciences, Beijing 100049, P. R. China*
†Electronic supplementary information (ESI) available. See DOI: https://doi.org/10.1039/d3nr05077g
‡These authors contributed equally to this work.

encourage us to continue exploring more possibilities for the Qx system.

However, the improvement of V_{OC} is usually accompanied by the sacrifice of other parameters. Therefore, it is essential to consider the trade-off between V_{OC} and J_{SC} × FF for high-performance OSCs. Side-chain engineering is also considered as an effective strategy to improve the performance of NFAs.[38] By introducing a large 2-butyloctyl branched alkyl chain at the β position of the thiophene unit, the resulting NFA L8-BO exhibited not only a higher V_{OC} but also a higher FF compared with Y6.[39] The branched alkyl chain at the β position of the thiophene unit has two key functions. Firstly, the branched-chain can change the energy level and light absorption range of the molecule; secondly, it can fine-tune steric hindrance in the molecules, therefore adjusting the molecular aggregation form.[40] These characteristics encourage us to design NFAs by introducing branched alkyl chains into a high V_{OC} system. It remains to be explored whether branched alkyl chains exhibit comparable effects in Qx systems with high V_{OC}s.

Herein, based on large Qx central cores, with introduction of branched alkyl chains at the β thiophene position, we first synthesized two novel NFAs, named **Qx-BO-1** and **Qx-BO-2** (Fig. 1a). As a result, the devices based on PM6:**Qx-BO-1** and PM6:**Qx-BO-2** achieved extremely high V_{OC}s above 0.95 V with excellent nonradiative energy losses as small as 0.18 eV. However, the excessive blue-shifted absorption spectrum and suboptimal film morphology result in a decreased J_{SC} and FF, thereby affecting the PCEs of devices based on **Qx-BO-1** and **Qx-BO-2**, which are not so satisfactory. Subsequently, we attempted to decrease the size of the central core, resulting in the synthesis of **Qx-BO-3**. Interestingly, the PCE of PM6:**Qx-BO-3**-based devices has been significantly improved to 17.03% with a relatively high V_{OC} of 0.889 V, a higher J_{SC} of 24.76 mA cm^{-2}, and a higher FF of 77.39%. **Qx-BO-3** showed better planarity, which may be attributed to the smaller steric hindrance of the branched alkyl chain and the central core with a moderate size. Besides, the PM6:**Qx-BO-3** blend film showed a more suitable crystallinity and phase separation size, which is conducive to the generation and transport of charge carriers.[41] The more balanced carrier mobility, higher exciton separation efficiency, and charge collection efficiency of the PM6:**Qx-BO-3** blend film are also important factors for its excellent device performance. These results illustrated that fine adjustment of the size of the central core containing the outside chains of NFAs is necessary. Our work also provides a useful reference for the molecular design of quinoxaline-based non-fullerene acceptors in the future.

2. Results and discussion

Optical and electrochemical properties

Fig. 1a shows the chemical structure of three NFAs, and the synthetic routes of **Qx-BO-1**, **Qx-BO-2**, and **Qx-BO-3** are presented in Scheme S1.† The three NFAs share similar synthetic procedures, and different precursors were used for the synthesis of the central core unit. All products have been confirmed by ^{1}H-NMR, ^{13}C-NMR, the MALDI-TOF mass test and elemental analysis (Fig. S1–S6, S11–S13 and Table S12†). These molecules exhibited good solubility in common solvents. The optimal molecular geometries and dihedral angles of **Qx-BO-1**, **Qx-BO-2**, and **Qx-BO-3** were calculated using density functional

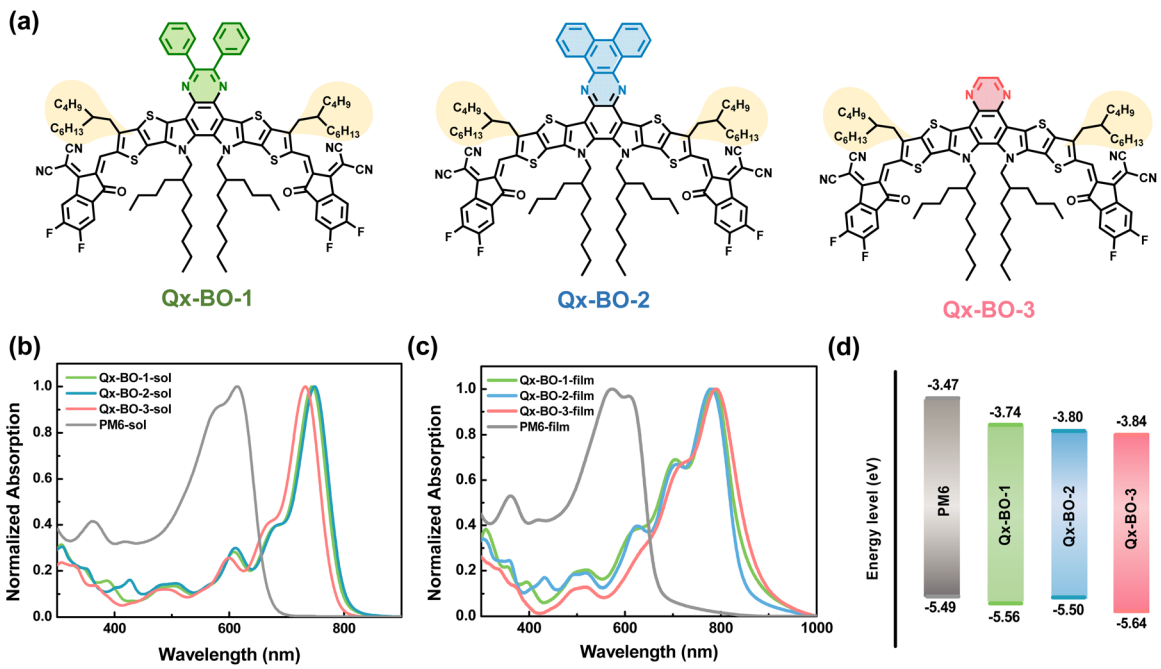

Fig. 1 (a) Chemical structures; (b) normalized solution absorption spectra; (c) normalized film absorption spectra; and (d) energy levels of PM6, **Qx-BO-1**, **Qx-BO-2**, and **Qx-BO-3**.

theory (DFT). For simplicity, we removed the alkyl chains on pyrrole units to obtain an optimized configuration. As shown in Fig. S7,† the molecular backbones of the three NFAs are all quasi-planar, enabling π-electrons to be well delocalized across the entire molecular backbone.[42] The dihedral angles between the central core and the terminal group of **Qx-BO-3** are 4.46° and 9.82°, which are smaller than those of **Qx-BO-1** and **Qx-BO-2** (4.71°, 12.46° and 4.70°, 12.89°). The interaction between the central core containing branched alkyl chains and the end group will affect the dihedral angle and then affect the planarity. The huge central cores of **Qx-BO-1** and **Qx-BO-2** make the molecules too crowded. Therefore, **Qx-BO-3** showed slightly better planarity, which can better regulate the compatibility with the donor in the thin film state.

The absorption spectra of PM6, **Qx-BO-1**, **Qx-BO-2** and **Qx-BO-3** in chloroform solution as well as in the solid state are presented in Fig. 1b and c, and the related optical parameters are outlined in Table S1.† When constructing OSC devices, three NFAs could form complementary absorption with PM6 in the light-absorbing active layers. In solution, these three NFAs showed almost the same absorption spectra. The maximum absorption peaks of them in neat film are located at 786, 775 and 791 nm. In addition, **Qx-BO-3** showed the most red-shifted absorption band edge at 881 nm in the thin film. From solutions to films, **Qx-BO-3** exhibited more remarkable red shifts (45 nm for **Qx-BO-1**, 37 nm for **Qx-BO-2**, and 94 nm for **Qx-BO-3**), which are attributed to the distinct aggregation and intermolecular interaction behavior of **Qx-BO-3** in the solid state. Moreover, compared to **Qx-BO-1** and **Qx-BO-2**, **Qx-BO-3** showed a higher film absorption coefficient (Fig. S14, S15 and Table S11†), which is conducive to obtaining a higher J_{SC} in devices. The optical bandgaps of **Qx-BO-1**, **Qx-BO-2** and **Qx-BO-3** were calculated to be 1.46 eV, 1.47 eV and 1.41 eV according to the formula $E_g^{opt} = 1240/\lambda_{onset}$. The molecular energy levels of these three NFAs were examined by cyclic voltammetry (CV) measurement (Fig. 1d and S8†). The lowest unoccupied molecular orbital (LUMO) and the highest occupied molecular orbital (HOMO) values of **Qx-BO-1**, **Qx-BO-2** and **Qx-BO-3** are 3.74/5.56 eV, 3.80/5.50 eV, and 3.84/5.64 eV, respectively, which were calculated according to the established formulas: $E_{HOMO} = -e(E_{OX} - E_{Fc/Fc^+} + 4.8)$ and $E_{LUMO} = -e(E_{RE} - E_{Fc/Fc^+} + 4.8)$. From **Qx-BO-1** to **Qx-BO-3**, the slightly downshifted LUMO values could be related to the reduction of the conjugated aromatic rings and also to the weak electron-donating properties of the benzene ring. The results indicated that **Qx-BO-1** and **Qx-BO-2** possess smaller charge transfer driving forces and nonradiative energy losses, which will be discussed in detail later.

Device performance

To study the influence of different central core size effects on the device performance, OSCs were fabricated based on the device structure of ITO/PEDOT:PSS/active layer/PNDIT-F3N/Ag. The detailed fabrication process and optimization data are displayed in Tables S2–S4.† As shown in Fig. 2a and Table 1, the **Qx-BO-1**-based devices showed a PCE of 10.57%, with a V_{OC} of 0.956 V, a J_{SC} of 18.21 mA cm^{-2} and an FF of 60.64%. As for the **Qx-BO-2**-based device, an increased V_{OC} value was obtained, which is up to 0.963 V. Compared with **Qx-BO-1** and **Qx-BO-2**, the PM6:**Qx-BO-3**-based device showed a notably elevated PCE of 17.03%, a J_{SC} of 24.76 mA cm^{-2} and an FF of 77.39%. Although the V_{OC} of the **Qx-BO-3**-based device has decreased to 0.889 V, it still belongs to the high level among those for high-performance Y-series NFAs in literature reports (Fig. S10 and Table S10†).[20,43–54] The overall photovoltaic performance has been significantly improved due to the higher J_{SC} and FF of the **Qx-BO-3**-based device. The external quantum efficiency (EQE) curves of the three devices are displayed in Fig. 2b. The devices based on PM6:**Qx-BO-3** exhibited a broad and strong photo-response in the range of 450–900 nm. The enlarged EQE values of **Qx-BO-3**-based devices should be ascribed to more efficient charge generation and transport. The calculated J_{SC} values from the EQE spectra were in good agreement with the J_{SC} values obtained in current density–voltage (J–V) measurements (within a 5% error). The scatter plots of V_{OC} and J_{SC} × FF value distribution of 16 independent measurements of OSCs based on the above three systems are displayed in Fig. 2c, intuitively showing that the improved J_{SC} and FF are the main reasons for the more efficient performances of PM6:**Qx-BO-3**-based devices.

To further reveal the reasons for the improvement of J_{SC} and FF in **Qx-BO-3**-based devices, it is necessary to explore the photophysical processes of the three systems. The relationship between the photogenerated current density J_{ph} and the effective voltage V_{eff} of the devices was first studied to understand exciton dissociation and collection of the devices (Fig. 2d). When the V_{eff} reaches 2 V, the exciton of the device will completely dissociate into free charge, so the current density of the device is the saturated current density J_{sat}. The exciton dissociation efficiency η_{diss} and charge collection efficiency η_{coll} of the device can be obtained by calculating the ratio of J_{ph} and J_{sat} under a short circuit and the maximum output power of the device.[55] The detailed data are summarized in Table S5.† Compared with PM6:**Qx-BO-1**-based devices and PM6:**Qx-BO-2**-based devices, PM6:**Qx-BO-3**-based devices showed higher η_{diss} and η_{coll} of 99.72% and 96.78%, respectively. The improved η_{diss} in PM6:**Qx-BO-3**-based OSCs may be related to their downshifted LUMO energy levels, which induced a larger driving force in theory for exciton dissociation.[56]

The dependence of J_{SC} and V_{OC} on the light intensity was investigated to reveal the charge recombination properties of the devices. Curves of J_{SC} *versus* light intensity for the three devices are shown in Fig. 2d, and the functional relationship between J_{SC} and P_{light} follows the formula $J_{SC} \propto (P_{light})^{\alpha}$. The closer the exponential factor (α) to 1, the lower the probability of bimolecular recombination and the higher the charge collection efficiency. Curves of V_{OC} *versus* light intensity for the devices are shown in Fig. 2e. The functional relationship between V_{OC} and P_{light} follows $V_{OC} \propto nkT/q \ln(P_{light})$, where k is the Boltzmann constant, T is the Kelvin temperature, and the closer the ideality factor (n) to 1, the lower the probability of

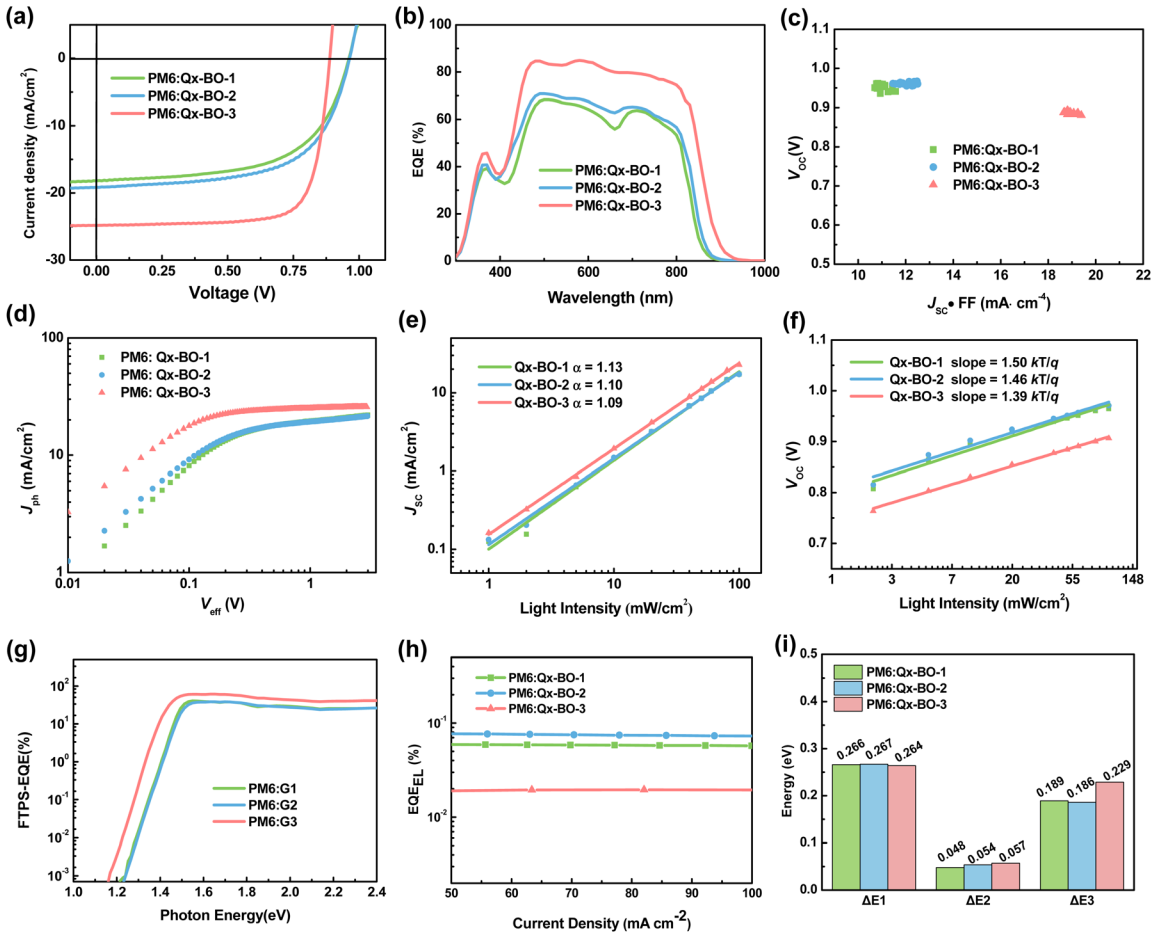

Fig. 2 (a) *J*–*V* curves of the corresponding optimized OSCs; (b) EQE curves; (c) V_{OC} and J_{SC} × FF values distribution scatter chart of 16 independently measured devices; (d) J_{ph} *versus* V_{eff} curves; (e) light intensity dependence of the J_{SC} values and (f) light intensity dependence of the V_{OC} values of the corresponding optimized devices; (g) FTPS-EQE spectra; (h) EQE_{EL} of the devices at different injection current densities; and (i) schematic of the radiative and nonradiative recombination losses.

Table 1 Optimal photovoltaic parameters of solar cells based on PM6:**Qx-BO-1**, PM6:**Qx-BO-2** and PM6:**Qx-BO-3**

Active layer	V_{OC} (V)	J_{SC} (mA cm^{-2})	FF (%)	PCE (%)	$J_{SC\text{-cal.}}$
PM6:**Qx-BO-1**	0.956 (0.956 ± 0.004)	18.21 (18.36 ± 0.40)	60.64 (59.80 ± 0.72)	10.57 (10.44 ± 0.18)[b]	17.53 (96.3%)[a]
PM6:**Qx-BO-2**	0.963 (0.961 ± 0.002)	19.18 (18.89 ± 0.24)	61.49 (60.91 ± 0.77)	11.34 (11.15 ± 0.15)	18.76 (97.8%)
PM6:**Qx-BO-3**	0.889 (0.887 ± 0.003)	24.76 (24.77 ± 0.25)	77.39 (76.49 ± 0.50)	17.03 (16.81 ± 0.14)	23.85 (96.3%)

[a] The integrated J_{SC} values in parentheses were calculated from the EQE spectra. [b] The average PCEs in parentheses were calculated from 20 devices.

trap-assisted recombination of the devices. The α of the PM6:**Qx-BO-3**-based device is 1.09, and the n is 1.39, which are closer to 1 than those of the PM6:**Qx-BO-1**-based device (α = 1.10 and n = 1.46) and the PM6:**Qx-BO-2**-based device (α = 1.13 and n = 1.50), indicating that the bimolecular and geminate recombination degree of the PM6:**Qx-BO-3**-based device is lower, thus resulting in more efficient photodynamic processes.

The hole and electron transport properties of the OSCs were investigated using the space charge limited current (SCLC) method (Fig. S9†), and the results are summarized in Table S6.† The electron mobilities (μ_e)/hole mobilities (μ_h) of the PM6:**Qx-BO-1**, PM6:**Qx-BO-2**, and PM6:**Qx-BO-3** blend films were 1.67 × 10^{-4}/3.56 × 10^{-4} cm^2 V^{-1} s^{-1}, 2.75 × 10^{-4}/3.92 × 10^{-4} cm^2 V^{-1} s^{-1}, and 7.04 × 10^{-4}/8.31 × 10^{-4} cm^2 V^{-1} s^{-1}, respectively. The μ_h/μ_e ratio of the PM6:**Qx-BO-1**, PM6:**Qx-BO-2** and PM6:**Qx-BO-3** blend films varies from large to small with the corresponding values of 2.13, 1.42 and 0.85. The results indicated that the PM6:**Qx-BO-3** blend films exhibited slightly higher and more balanced hole and electron mobilities, which

is favorable for charge transport and collection and can well explain the higher J_{SC} and FF of the PM6:**Qx-BO-3**-based devices.[57]

Noting that the V_{OC} values of the PM6:**Qx-BO-1** and PM6:**Qx-BO-2**-based devices were much higher than that of the PM6:**Qx-BO-3**-based devices, E_{loss} tests on the devices of the three systems were conducted respectively (Fig. 2g–i). According to the Shockley–Queisser (SQ) limit, the E_{loss} in OSCs can be divided into three parts: $E_{loss} = E_g - qV_{OC} = \Delta E_1 + \Delta E_2 + \Delta E_3$, where E_g is the photovoltaic energy bandgap extracted from the derivation of the EQE_{PV} curve.[58] ΔE_1 is the energy loss due to the radiative recombination above the optical gap, which is unavoidable for any sort of solar cell.[59] The ΔE_1 values of the three NFA-based devices are almost the same (0.26 eV). The generation of ΔE_2 is due to radiation recombination losses below the band gap. The small ΔE_2 of the three NFA-based devices was about 0.05 eV, indicating that the radiation recombination loss was not significant. The third part, ΔE_3, was caused by nonradiative recombination and can be calculated as $\Delta E_3 = k_B T \ln(EQE_{EL})$, where EQE_{EL} represents the radiation quantum efficiency of the OSCs under dark current conditions. As shown in Fig. 2i and Table S7,† the ΔE_3 values of the PM6:**Qx-BO-1**, PM6:**Qx-BO-2**, and PM6:**Qx-BO-3**-based devices are 0.189, 0.186, and 0.229 eV, respectively. The nonradiative E_{loss}s of most systems are larger than 0.2 eV.[48,60] In summary, although the E_{loss} of the PM6:**Qx-BO-3**-based device was the largest, it achieved a better balance among J_{SC}, V_{OC}, and FF due to its efficient charge generation and transport properties, thus obtaining the most efficient OSCs. At the same time, the stability test results show that (Fig. S16†), after 1000 hours of illumination, the PM6:Qx-BO and PM6:Y6-based devices almost maintained more than 80% of the initial PCE, indicating that the Qx-BO series acceptors have relatively good photostability.

Morphology characterization

To investigate the influence of different sized central core substitutions on the active layer morphology, atomic force microscopy (AFM) and transmission electron microscopy (TEM) were performed. As illustrated in Fig. 3a, significantly different surface morphologies can be observed for the three blend films from the AFM images. The root-mean-square roughness decreased from PM6:**Qx-BO-1** to PM6:**Qx-BO-3** blend films (PM6:**Qx-BO-1**, 4.30 nm; PM6:**Qx-BO-2**, 2.54 nm; and PM6:**Qx-BO-3**, 1.03 nm). Generally, the lower the roughness, the more favorable the contact between the blend film

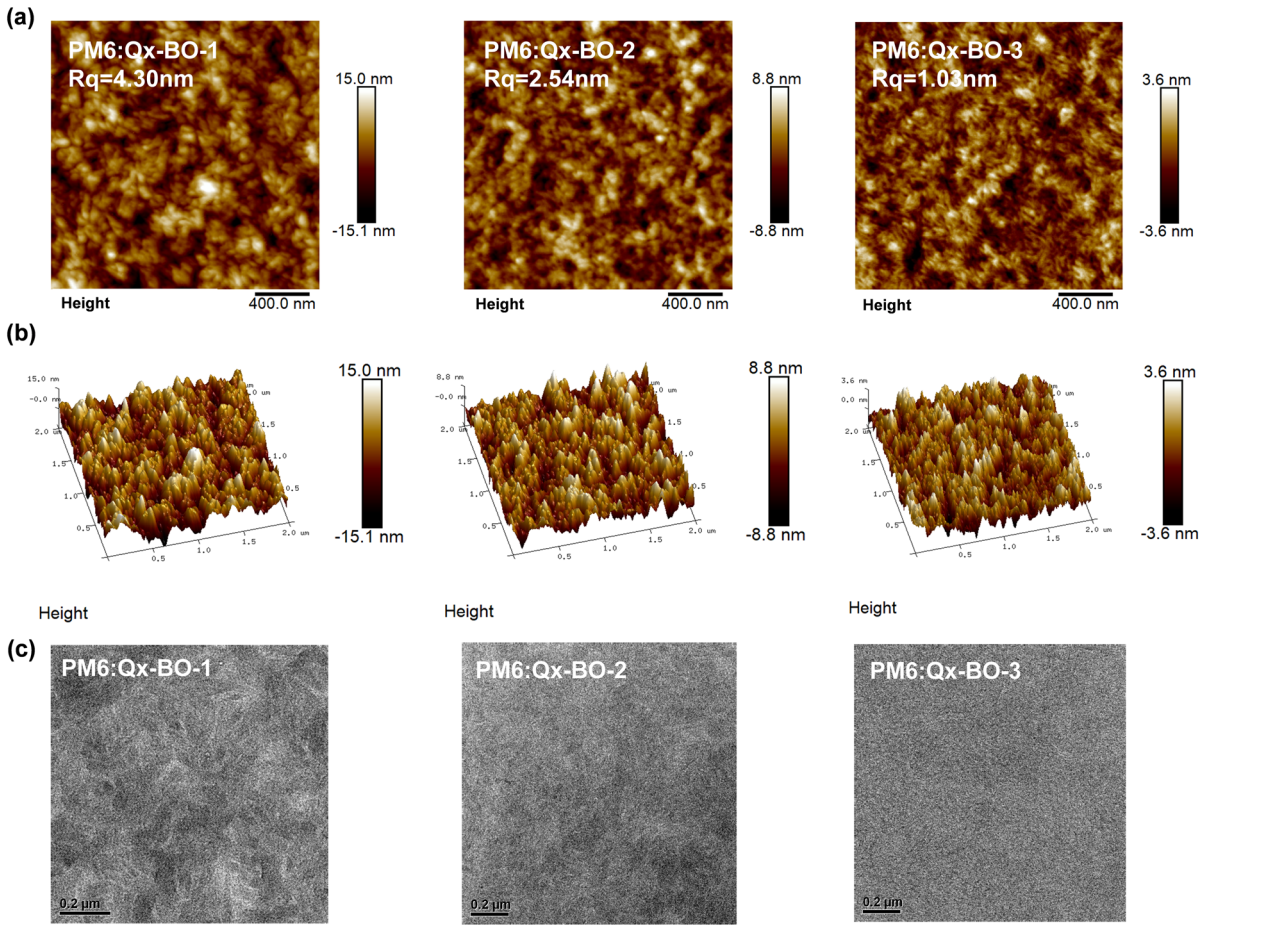

Fig. 3 (a and b) AFM height images and (c) TEM images of PM6:**Qx-BO-1**, PM6:**Qx-BO-2**, and PM6:**Qx-BO-3** blend films.

and the transport layer and the electrode.[61] In addition, the PM6:**Qx-BO-3** blend film showed a nanoscale interpenetrating network with a tiny fibrous structure, which greatly promotes exciton separation and carrier transport.[62] As shown in the TEM images (Fig. 3c), the PM6:**Qx-BO-1** blend film exhibited a large phase separation with an alternate light and dark region of about several tens of nanometers, ascribed to the crystallinity of the PM6:**Qx-BO-1** blend film which is too strong, which may lead to a lower J_{SC} and FF of the PM6:**Qx-BO-1** based devices. In contrast, the PM6:**Qx-BO-3** blend film has a fairly uniform surface with appropriate crystallinity and phase separation scale. Within a certain range, it provides more donor and acceptor interfaces for the efficient dissociation of excitons, thus resulting in a higher and more balanced carrier mobility of the PM6:**Qx-BO-3**-based devices.[63]

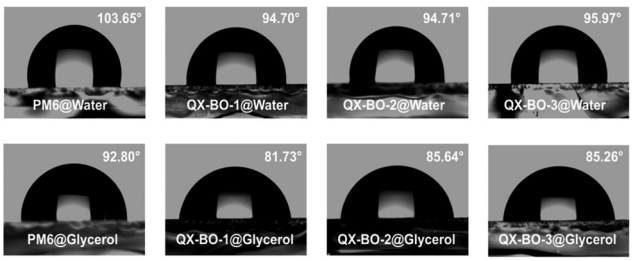

Fig. 4 Images of water and glycerol drops on the PM6, **Qx-BO-1**, **Qx-BO-2**, and **Qx-BO-3** films.

Considering that the adjustment of the molecular structure of NFAs possesses a significant impact on the membrane morphology, the contact angle test was used to explore the compatibility of the donor and acceptor. Fig. 4 shows the contact angle of water and glycerol drops on the surface of the **Qx-BO-1**, **Qx-BO-2**, **Qx-BO-3**, and PM6 films. The surface tension (γ) values are 15.98, 15.35, 14.81 and 11.82 mN m^{-1}, respectively. Detailed data are displayed in Table S8.† The results showed that the surface tension of **Qx-BO-3** and PM6 is closer, and the interaction parameter χ of the PM6:**Qx-BO-3** system is calculated to be 0.17, indicating that there is good miscibility between **Qx-BO-3** and PM6. When the size of the central core becomes larger, the interaction parameter between the donor and the acceptor increases (0.31 for **Qx-BO-1** and 0.23 for **Qx-BO-2**), which means that the miscibility between the donor and the acceptor becomes poor, leading to excessive aggregation in the film. The suitable compatibility performance further explained the relatively homogeneous morphology without any objective large-size phase separation of the PM6:**Qx-BO-3** blend film.

Additionally, to further study the molecular stacking behavior and crystallization of the blend films, the grazing-incidence wide-angle X-ray scattering (GIWAXS) test was conducted. The 2D GIWAXS images of single component and blended films are presented in Fig. 5. As shown in Fig. 5a and c, it can be observed that the three systems exhibited significant face-on molecular orientation. The ordered face-on stacking in the blend films can greatly facilitate charge transport.[64] Fig. 5b and d show one-dimensional linear maps extracted from two-

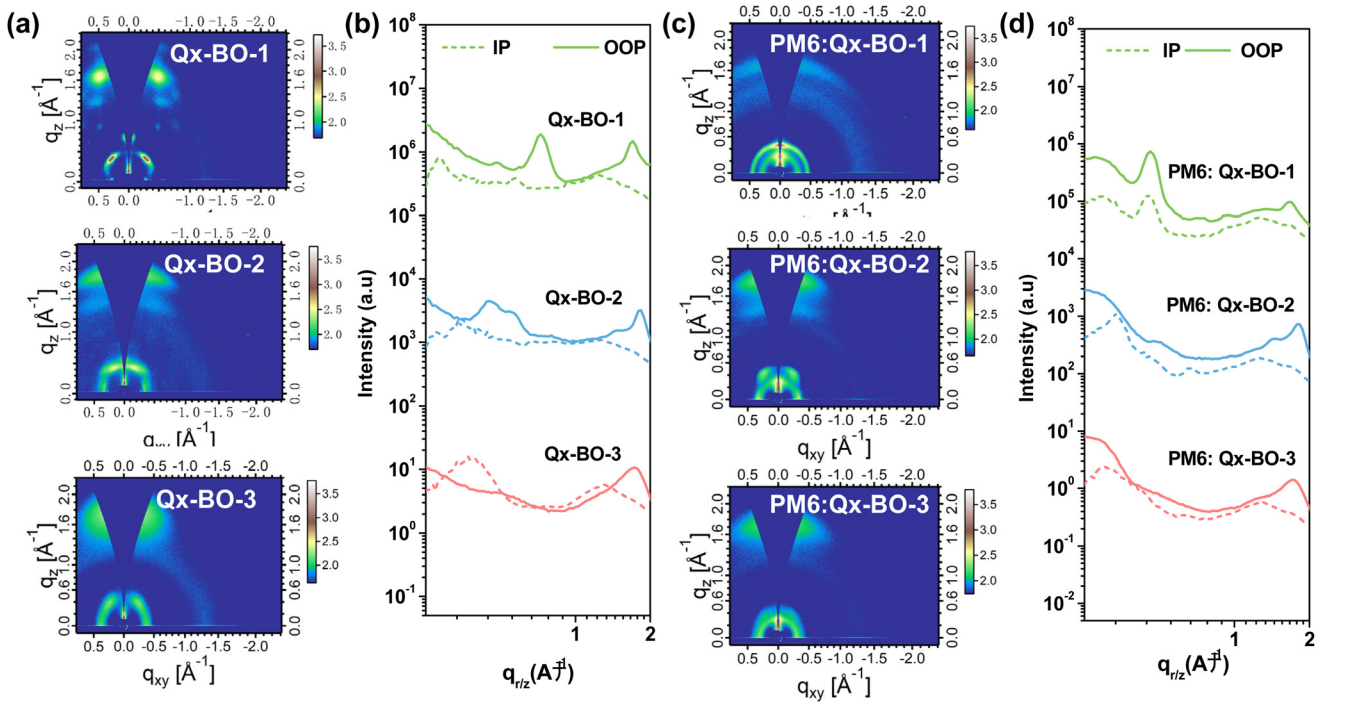

Fig. 5 (a) Two-dimensional GIWAXS patterns of neat films; (b) in-plane (solid lines) and out-of-plane (dashed lines) cuts of neat films; (c) two-dimensional GIWAXS patterns of the blend films; and (d) in-plane (solid lines) and out-of-plane (dashed lines) cuts of blend films.

dimensional maps. The π–π stacking peak of the PM6:**Qx-BO-3** blend film in the (010) direction is located at q_z = 1.69 Å^{-1}, which is a strong peak in the out-of-plane (OOP) direction (d = 3.72 Å). According to the Scherrer calculation, the crystal coherence lengths (CCL) in the (010) direction of the three systems are presented in Table S9.† [65] **Qx-BO-3** showed smaller CCL values in both neat and blend films (13.81 Å for the neat film, 15.44 Å for the blend film). If the three NFAs are compared horizontally, whether in a single component or a blend film, the CCL of **Qx-BO-3** is much smaller than those of **Qx-BO-1** and **Qx-BO-2**. This indicated that the crystallinity of **Qx-BO-3** is weaker than that of the other two NFAs, so the appearance of too large phase regions is avoided during the film formation process. In addition, compared with **Qx-BO-3**, the relatively poor solubility of **Qx-BO-1** and **Qx-BO-2** leads to pre-aggregation in the process of rapid film formation, which leads to too strong crystallinity and too large phase size. After blending with donor PM6, the crystallinity of **Qx-BO-3** improved which exhibited a better ability to maintain crystallization, which also conforms to the results that **Qx-BO-3** has good compatibility with PM6. However, after blending with PM6, the CCL of **Qx-BO-1** and **Qx-BO-2** decreased. This may be due to the insertion of PM6 during the molecular stacking process destroying the pre-aggregation of the acceptor molecules, resulting in reduced crystallinity. In summary, the PM6:**Qx-BO-3** blend film showed better nanoscale aggregation and more appropriate molecular stacking, which could promote charge transport and improve the photovoltaic performance.

3. Conclusion

In this work, three NFAs, **Qx-BO-1**, **Qx-BO-2**, and **Qx-BO-3**, with different sizes of quinoxaline central cores and β-branched alkyl chains were designed and synthesized. Compared with **Qx-BO-3**, the central core sizes of **Qx-BO-1** and **Qx-BO-2** were larger, and the high energy level and low E_{loss} of **Qx-BO-1** and **Qx-BO-2** led to their V_{OC} reaching above 0.95 V, but both J_{SC} and FF were lower, resulting in sub-optimal PCEs of only 10.57% and 11.34%. This is because the larger central core size deteriorates the aggregation morphology and affects the photophysical process, and the steric hindrance of the central core size in **Qx-BO-3** decreases when a smaller quinoxaline unit is used as the central core, which effectively optimizes the nanophase separation scale and film morphology, resulting in a more balanced carrier mobility. As a result, the PCE of devices based on PM6:**Qx-BO-3** is 17.03%, the V_{OC} is 0.889 V, the J_{SC} is 24.76 mA cm^{-2}, and the FF is 77.39%. Balanced carrier mobility, appropriate crystallization performance, and phase separation size are comprehensive factors to improve the photovoltaic performance of the PM6:**Qx-BO-3**-based devices. These results indicated that the size of central cores containing huge branched alkyl chains needs to be further adjusted to obtain better nanoscale morphology, which is beneficial for exciton separation and charge transfer and collection. In summary, this work puts forward a feasible strategy to construct efficient non-fullerene acceptors by reasonably utilizing the central core size effect.

Author contributions

Xinya Ran: conceptualization, data curation, formal analysis, investigation, methodology, validation, writing – original draft, and writing – review & editing. Yanan Shi: investigation and validation. Dingding Qiu: investigation. Jianqi Zhang: investigation. Kun Lu: conceptualization, funding acquisition, project administration, project administration, resources, supervision, and writing – review & editing. Zhixiang Wei: funding acquisition, project administration, resources, supervision, and writing – review & editing.

Conflicts of interest

The authors declare no conflict of interest.

Acknowledgements

We acknowledge the financial support provided by the National Natural Science Foundation of China (Grant No. 51973043) and the Strategic Priority Research Program of the Chinese Academy of Sciences (no. XDB36000000). The authors thank Qun Luo and Xingze Chen from Suzhou Nanometer Institute for their assistance in photostability testing.

References

1 L. Ma, S. Zhang, J. Ren, G. Wang, J. Li, Z. Chen, H. Yao and J. Hou, *Angew. Chem., Int. Ed.*, 2023, **62**, e202214088.
2 J. Ren, P. Bi, J. Zhang, J. Liu, J. Wang, Y. Xu, Z. Wei, S. Zhang and J. Hou, *Natl. Sci. Rev.*, 2021, **8**, nwab031.
3 Y. F. Shen, H. Zhang, J. Zhang, C. Tian, Y. Shi, D. Qiu, Z. Zhang, K. Lu and Z. Wei, *Adv. Mater.*, 2023, **35**, e2209030.
4 H. Chen, S. Y. Jeong, J. Tian, Y. Zhang, D. R. Naphade, M. Alsufyani, W. Zhang, S. Griggs, H. Hu, S. Barlow, H. Y. Woo, S. R. Marder, T. D. Anthopoulos, I. McCulloch and Y. Lin, *Energy Environ. Sci.*, 2023, **16**, 1062–1070.
5 T. Chen, S. Wang, Z. Yang, Q. Feng, X. Sun, L. Li, Z. S. Wang and H. Peng, *Angew. Chem., Int. Ed.*, 2011, **50**, 1815–1819.
6 J. Zhao, Y. Li, G. Yang, K. Jiang, H. Lin, H. Ade, W. Ma and H. Yan, *Nat. Energy*, 2016, **1**, 15027.
7 H. Tang, Y. Bai, H. Zhao, X. Qin, Z. Hu, C. Zhou, F. Huang and Y. Cao, *Adv. Mater.*, 2023, e2212236.
8 Z. Zheng, J. Wang, P. Bi, J. Ren, Y. Wang, Y. Yang, X. Liu, S. Zhang and J. Hou, *Joule*, 2022, **6**, 171–184.
9 M. Deng, X. Xu, Y. Duan, L. Yu, R. Li and Q. Peng, *Adv. Mater.*, 2023, **35**, e2210760.

10 J. Ge, Z. Chen, Q. Ye, L. Xie, W. Song, Y. Guo, J. Zhang, X. Tong, J. Zhang, E. Zhou, Z. Wei and Z. Ge, *ACS Appl. Mater. Interfaces*, 2023, **15**, 10803–10811.
11 Y. Shi, J. Pan, J. Yu, J. Zhang, F. Gao, K. Lu and Z. Wei, *Sol. RRL*, 2021, **5**, 2100008.
12 C. Xiao, X. Wang, T. Zhong, R. Zhou, X. Zheng, Y. Liu, T. Hu, Y. Luo, F. Sun, B. Xiao, Z. Liu, C. Yang and R. Yang, *Adv. Sci.*, 2023, **10**, e2206580.
13 Y. Chang, X. Zhu, Y. Shi, Y. Liu, K. Meng, Y. Li, J. Xue, L. Zhu, J. Zhang, H. Zhou, W. Ma, Z. Wei and K. Lu, *Energy Environ. Sci.*, 2022, **15**, 2937–2947.
14 Y. Shi, Y. Chang, K. Lu, Z. Chen, J. Zhang, Y. Yan, D. Qiu, Y. Liu, M. A. Adil, W. Ma, X. Hao, L. Zhu and Z. Wei, *Nat. Commun.*, 2022, **13**, 3256.
15 W. Gao, F. Qi, Z. Peng, F. R. Lin, K. Jiang, C. Zhong, W. Kaminsky, Z. Guan, C. S. Lee, T. J. Marks, H. Ade and A. K. Jen, *Adv. Mater.*, 2022, **34**, e2202089.
16 C. He, Y. Pan, Y. Ouyang, Q. Shen, Y. Gao, K. Yan, J. Fang, Y. Chen, C.-Q. Ma, J. Min, C. Zhang, L. Zuo and H. Chen, *Energy Environ. Sci.*, 2022, **15**, 2537–2544.
17 P. Cong, X. Li, A. Tang, J. Wu, J. Chen, L. Chen and E. Zhou, *Chem. Commun.*, 2022, **58**, 13373–13376.
18 T. Dai, X. Li, P. Lei, A. Tang, Y. Geng, Q. Zeng and E. Zhou, *Nano Energy*, 2022, **99**, 3256.
19 T. Dai, A. Tang, Z. He, M. Du, P. Lei, Q. Zeng, Z. Wang, Y. Wang, S. Lu, Y. Zhong and E. Zhou, *Energy Environ. Sci.*, 2023, **16**, 2199–2211.
20 J. Yuan, Y. Zhang, L. Zhou, G. Zhang, H.-L. Yip, T.-K. Lau, X. Lu, C. Zhu, H. Peng, P. A. Johnson, M. Leclerc, Y. Cao, J. Ulanski, Y. Li and Y. Zou, *Joule*, 2019, **3**, 1140–1151.
21 Y. Cui, H. Yao, J. Zhang, K. Xian, T. Zhang, L. Hong, Y. Wang, Y. Xu, K. Ma, C. An, C. He, Z. Wei, F. Gao and J. Hou, *Adv. Mater.*, 2020, **32**, e1908205.
22 P. Murugan, T. Hu, X. Hu and Y. Chen, *J. Mater. Chem. A*, 2022, **10**, 17968–17987.
23 M. Du, Y. Xiao, Y. Geng, Y. Chen, H. Jiang, C. Dong, Q. Guo, Q. Guo, G. Li and E. Zhou, *J. Mater. Chem. C*, 2022, **10**, 10114–10123.
24 X. Kong, C. Zhu, J. Zhang, L. Meng, S. Qin, J. Zhang, J. Li, Z. Wei and Y. Li, *Energy Environ. Sci.*, 2022, **15**, 2011–2020.
25 Y. Gao, Q. Chen, L. Wang, H. Huang, A. Zhang, C. Li, X. Xu and Z. Bo, *J. Mater. Chem. C*, 2022, **10**, 10389–10395.
26 S. Chen, L. Hong, M. Dong, W. Deng, L. Shao, Y. Bai, K. Zhang, C. Liu, H. Wu and F. Huang, *Angew. Chem., Int. Ed.*, 2023, **62**, e202213869.
27 Y. Chen, R. Ma, T. Liu, Y. Xiao, H. K. Kim, J. Zhang, C. Ma, H. Sun, F. Bai, X. Guo, K. S. Wong, X. Lu and H. Yan, *Adv. Energy Mater.*, 2021, **11**, 2003777.
28 G.-Z. Yuan, H. Fan, S.-S. Wan, Z. Jiang, Y.-Q. Liu, K.-K. Liu, H.-R. Bai, X. Zhu and J.-L. Wang, *J. Mater. Chem. A*, 2019, **7**, 20274–20284.
29 L. Xie, A. Lan, Q. Gu, S. Yang, W. Song, J. Ge, R. Zhou, Z. Chen, J. Zhang, X. Zhang, D. Yang, B. Tang, T. Wu and Z. Ge, *ACS Energy Lett.*, 2022, **8**, 361–371.
30 J. Yuan, Y. Zhang, L. Zhou, C. Zhang, T. K. Lau, G. Zhang, X. Lu, H. L. Yip, S. K. So, S. Beaupre, M. Mainville, P. A. Johnson, M. Leclerc, H. Chen, H. Peng, Y. Li and Y. Zou, *Adv. Mater.*, 2019, **31**, e1807577.
31 M. Chang, Y. Zhang, B.-S. Lu, D. Sui, F. Wang, J. Wang, Y. Yang and B. Kan, *Chem. Eng. J.*, 2022, **427**, 131473.
32 B. Sun, Y. Chen, Y. Huang, Y. Li and J. Fan, *Org. Electron.*, 2021, **98**, 106282.
33 B. Xie, S. Bi, R. Wu, L. Yin, C. Ji, Z. Cai and Y. Li, *RSC Adv.*, 2017, **7**, 23779–23786.
34 Y. Yan, Y. Zhang, Y. Liu, Y. Shi, D. Qiu, D. Deng, J. Zhang, B. Wang, M. A. Adil, K. Amin, W. A. Memon, M. Wang, H. Zhou, X. Zhang and Z. Wei, *Adv. Energy Mater.*, 2022, **12**, 2200129.
35 H. Chen, Y. Zou, H. Liang, T. He, X. Xu, Y. Zhang, Z. Ma, J. Wang, M. Zhang, Q. Li, C. Li, G. Long, X. Wan, Z. Yao and Y. Chen, *Sci. China: Chem.*, 2022, **65**, 1362–1373.
36 Z. Zhou, W. Liu, G. Zhou, M. Zhang, D. Qian, J. Zhang, S. Chen, S. Xu, C. Yang, F. Gao, H. Zhu, F. Liu and X. Zhu, *Adv. Mater.*, 2020, **32**, e1906324.
37 Y. Shi, Y. Chang, K. Lu, Z. Chen, J. Zhang, Y. Yan, D. Qiu, Y. Liu, M. A. Adil, W. Ma, X. Hao, L. Zhu and Z. Wei, *Nat. Commun.*, 2022, **13**, 3256.
38 Z. Luo, Y. Gao, H. Lai, Y. Li, Z. Wu, Z. Chen, R. Sun, J. Ren, C. Zhang, F. He, H. Woo, J. Min and C. Yang, *Energy Environ. Sci.*, 2022, **15**, 4601–4611.
39 H. Ji, J. Li, M. Du, J. Yang, A. Tang, G. Li, Q. Guo and E. Zhou, *J. Phys. Chem. C*, 2021, **125**, 10876–10882.
40 Q. Wang, Z. Hu, Z. Wu, Y. Lin, L. Zhang, L. Liu, Y. Ma, Y. Cao and J. Chen, *ACS Appl. Mater. Interfaces*, 2020, **12**, 4659–4672.
41 R. Zheng, C. Zhang, A. Zhang, J. Xue, X. Xu, Y. Liu, C. J. Su, W. Ma, C. Yang and Z. Bo, *ACS Appl. Mater. Interfaces*, 2023, **15**, 4275–4283.
42 W. Zhu, A. P. Spencer, S. Mukherjee, J. M. Alzola, V. K. Sangwan, S. H. Amsterdam, S. M. Swick, L. O. Jones, M. C. Heiber, A. A. Herzing, G. Li, C. L. Stern, D. M. DeLongchamp, K. L. Kohlstedt, M. C. Hersam, G. C. Schatz, M. R. Wasielewski, L. X. Chen, A. Facchetti and T. J. Marks, *J. Am. Chem. Soc.*, 2020, **142**, 14532–14547.
43 H. Chen, H. Liang, Z. Guo, Y. Zhu, Z. Zhang, Z. Li, X. Cao, H. Wang, W. Feng, Y. Zou, L. Meng, X. Xu, B. Kan, C. Li, Z. Yao, X. Wan, Z. Ma and Y. Chen, *Angew. Chem., Int. Ed.*, 2022, **61**, e202209580.
44 Y. Cui, H. Yao, J. Zhang, K. Xian, T. Zhang, L. Hong, Y. Wang, Y. Xu, K. Ma, C. An, C. He, Z. Wei, F. Gao and J. Hou, *Adv. Mater.*, 2020, **32**, 1908205.
45 S. Li, Q. Fu, L. Meng, X. Wan, L. Ding, G. Lu, G. Lu, Z. Yao, C. Li and Y. Chen, *Angew. Chem., Int. Ed.*, 2022, **61**, e202207397.
46 S. Li, L. Zhan, N. Yao, X. Xia, Z. Chen, W. Yang, C. He, L. Zuo, M. Shi, H. Zhu, X. Lu, F. Zhang and H. Chen, *Nat. Commun.*, 2021, **12**, 4627.
47 H. Liu, T. Dai, J. Zhou, H. Wang, Q. Guo, Q. Guo and E. Zhou, *Nano Res.*, 2023, DOI: **10.1007/s12274-023-5693-z**.
48 S. Liu, J. Yuan, W. Deng, M. Luo, Y. Xie, Q. Liang, Y. Zou, Z. He, H. Wu and Y. Cao, *Nat. Photonics*, 2020, **14**, 300–305.

49 X. Ma, J. Wang, J. Gao, Z. Hu, C. Xu, X. Zhang and F. Zhang, *Adv. Energy Mater.*, 2020, **10**, 2001404.
50 Y. Pan, X. Zheng, J. Guo, Z. Chen, S. Li, C. He, S. Ye, X. Xia, S. Wang, X. Lu, H. Zhu, J. Min, L. Zuo, M. Shi and H. Chen, *Adv. Funct. Mater.*, 2021, **32**, 2108614.
51 J. Zhang, F. Bai, I. Angunawela, X. Xu, S. Luo, C. Li, G. Chai, H. Yu, Y. Chen, H. Hu, Z. Ma, H. Ade and H. Yan, *Adv. Energy Mater.*, 2021, **11**, 2102596.
52 Z. Zhou, W. Liu, G. Zhou, M. Zhang, D. Qian, J. Zhang, S. Chen, S. Xu, C. Yang, F. Gao, H. Zhu, F. Liu and X. Zhu, *Adv. Mater.*, 2019, **32**, 1906324.
53 C. Zhu, J. Yuan, F. Cai, L. Meng, H. Zhang, H. Chen, J. Li, B. Qiu, H. Peng, S. Chen, Y. Hu, C. Yang, F. Gao, Y. Zou and Y. Li, *Energy Environ. Sci.*, 2020, **13**, 2459–2466.
54 Y. Zou, H. Chen, X. Bi, X. Xu, H. Wang, M. Lin, Z. Ma, M. Zhang, C. Li, X. Wan, G. Long, Y. Zhaoyang and Y. Chen, *Energy Environ. Sci.*, 2022, **15**, 4000.
55 V. D. Mihailetchi, L. J. Koster, J. C. Hummelen and P. W. Blom, *Phys. Rev. Lett.*, 2004, **93**, 216601.
56 J. Liu, S. Chen, D. Qian, B. Gautam, G. Yang, J. Zhao, J. Bergqvist, F. Zhang, W. Ma, H. Ade, O. Inganäs, K. Gundogdu, F. Gao and H. Yan, *Nat. Energy*, 2016, **1**, 16089.
57 P. W. M. Blom, M. J. M. de Jong and J. J. M. Vleggaar, *Appl. Phys. Lett.*, 1996, **68**, 3308–3310.
58 D. Qian, Z. Zheng, H. Yao, W. Tress, T. R. Hopper, S. Chen, S. Li, J. Liu, S. Chen, J. Zhang, X. K. Liu, B. Gao, L. Ouyang, Y. Jin, G. Pozina, I. A. Buyanova, W. M. Chen, O. Inganas, V. Coropceanu, J. L. Bredas, H. Yan, J. Hou, F. Zhang, A. A. Bakulin and F. Gao, *Nat. Mater.*, 2018, **17**, 703–709.
59 J. Benduhn, K. Tvingstedt, F. Piersimoni, S. Ullbrich, Y. Fan, M. Tropiano, K. A. McGarry, O. Zeika, M. K. Riede, C. J. Douglas, S. Barlow, S. R. Marder, D. Neher, D. Spoltore and K. Vandewal, *Nat. Energy*, 2017, **2**, 17053.
60 J. Wang, H. Chen, X. Xu, Z. Ma, Z. Zhang, C. Li, Y. Yang, J. Wang, Y. Zhao, M. Zhang, X. Wan, Y. Lu and Y. Chen, *J. Mater. Chem. A*, 2022, **10**, 16714–16721.
61 T. Liu, L. Huo, S. Chandrabose, K. Chen, G. Han, F. Qi, X. Meng, D. Xie, W. Ma, Y. Yi, J. M. Hodgkiss, F. Liu, J. Wang, C. Yang and Y. Sun, *Adv. Mater.*, 2018, **30**, e1707353.
62 H. Chen, T. Zhao, L. Li, P. Tan, H. Lai, Y. Zhu, X. Lai, L. Han, N. Zheng, L. Guo and F. He, *Adv. Mater.*, 2021, **33**, e2102778.
63 J. Fang, D. Deng, Z. Wang, M. A. Adil, T. Xiao, Y. Wang, G. Lu, Y. Zhang, J. Zhang, W. Ma and Z. Wei, *ACS Appl. Mater. Interfaces*, 2018, **10**, 12913–12920.
64 Y. Wang, X. Wang, B. Lin, Z. Bi, X. Zhou, H. B. Naveed, K. Zhou, H. Yan, Z. Tang and W. Ma, *Adv. Energy Mater.*, 2020, **10**, 2000826.
65 L. Ye, K. Weng, J. Xu, X. Du, S. Chandrabose, K. Chen, J. Zhou, G. Han, S. Tan, Z. Xie, Y. Yi, N. Li, F. Liu, J. M. Hodgkiss, C. J. Brabec and Y. Sun, *Nat. Commun.*, 2020, **11**, 6005.